INL/CON-07-12067
PREPRINT

# Measurement of Turbulent Flow Phenomena for the Lower Plenum of a Prismatic Gas-Cooled Reactor

## 12th International Topical Meeting on Nuclear Reactor Thermal Hydraulics (NURETH-12)

Hugh M. McIlroy, Jr.
Donald M. McEligot
Robert J. Pink

September 2007



# MEASUREMENT OF TURBULENT FLOW PHENOMENA FOR THE LOWER PLENUM OF A PRISMATIC GAS-COOLED REACTOR

**Hugh M. McIlroy Jr., Donald M. McEligot,* and Robert J. Pink**
Idaho National Laboratory
P.O. Box 1625
Idaho Falls, Idaho 83415
Hugh.McIlroy@inl.gov; Robert.Pink@inl.gov

## ABSTRACT

Mean-velocity-field and turbulence data are presented that measure turbulent flow phenomena in an approximately 1:7 scale model of a region of the lower plenum of a typical prismatic gas-cooled reactor (GCR) similar to a General Atomics design (Gas-Turbine-Modular Helium Reactor). The data were obtained in the Matched-Index-of-Refraction (MIR) facility at Idaho National Laboratory (INL) and are offered as a benchmark for assessing computational fluid dynamics (CFD) software. This experiment has been selected as the first Standard Problem endorsed by the Generation IV International Forum. The *primary objective* of this paper is to *document the experiment and present a sample of the data set* that has been established for this standard problem.

Present results concentrate on the region of the lower plenum near its far reflector wall (away from the outlet duct). The flow in the lower plenum consists of multiple jets injected into a confined cross flow - with obstructions. The model consists of a row of full circular posts along its centerline with half-posts on the two parallel walls to approximate flow scaled to that expected from the staggered parallel rows of posts in the reactor design. Posts, side walls and end walls are fabricated from clear, fused quartz to match the refractive-index of the mineral oil working fluid so that optical techniques may be employed for the measurements. The benefit of the MIR technique is that it permits optical measurements to determine flow characteristics in complex passages and around objects to be obtained without locating intrusive transducers that will disturb the flow field and without distortion of the optical paths. An advantage of the INL system is its large size, leading to improved spatial and temporal resolution compared to similar facilities at smaller scales. A three-dimensional (3-D) Particle Image Velocimetry (PIV) system was used to collect the data. Inlet jet Reynolds numbers (based on the hydraulic diameter of the jet and the time-mean average flow rate) are approximately 4,300 and 12,400. Uncertainty analysis and a discussion of the standard problem are included.

The measurements reveal complicated flow patterns that include several large recirculation zones, reverse flow near the simulated reflector wall, recirculation zones in the upper portion of the plenum and complex flow patterns around the support posts. Data include three-dimensional PIV images of flow planes, data displays along the coordinate planes (slices) and presentations that describe the component flows at specific regions in the model.

* Professor Emeritus, University of Arizona and presently on sabbatical leave at IKE, University of Stuttgart

**KEYWORDS**
Multiple jets, confined crossflow, 3-D PIV, MIR Lab, GCR lower plenum

## 1. BACKGROUND

The Very High Temperature Reactor (VHTR) is a candidate for the Next Generation Nuclear Plant (NGNP). Because of the high outlet temperatures characteristic of the VHTR, it is important to be able to simulate the turbulent flow in the reactor, especially in the lower plenum where the coolant is hottest, in order to ensure that large temperature gradients are not present in the coolant that could adversely impact structural materials. It is recognized that to simulate the flow in the VHTR lower plenum, advanced CFD codes using appropriate turbulence modeling will be necessary. The VHTR design used as the basis for this study has prismatic core and outlet plenum characteristics similar to those designed by General Atomics, Inc.

## 2. INTRODUCTION

The objectives of the NGNP Methods Program that led to performing the experiments described in this paper are (1) to build numerical calculational models of the important VHTR thermal-fluids phenomena identified in the phenomenal identification and ranking tables (PIRT) to date; and (2) to demonstrate that the models have sufficient capability to calculate the important phenomena within a prescribed acceptance criteria by using high fidelity validation data. The experiment described herein was designed to deliver high-fidelity data to validate the capability of CFD software to calculate the turbulent behavior in the lower plenum of a gas-cooled reactor with a prismatic core.

For very high temperature gas-cooled reactors only CFD software has the capability to calculate the presence of localized hot spots and undesirable thermal gradients. Because the flow in the reactor lower plenum is turbulent and complex, the turbulence models available in CFD software will be used to calculate the expected behavior. Unfortunately, some turbulence models in general purpose CFD codes provide optimistic predictions in the sense that surface temperatures are typically underpredicted [1,2]. The U.S. Department of Energy (DOE) needs improved modeling capabilities, independent from the traditional approaches employed by reactor vendors. These computational capabilities need, in turn, to be validated by comparison to experimental and analytical benchmark data.

McEligot et al. [3] reported six areas of thermal hydraulic phenomena in which the application of improved CFD and system thermal-hydraulic analytical techniques can be used in the design and safety analyses of a prismatic VHTR. Several of these phenomena are pertinent to pebble bed versions of the VHTR as well. Initial studies concentrate on coolant flow distribution through the reactor core channels and mixing of hot jets in the reactor core lower plenum. These phenomena are important both in normal operation and in accident scenarios. This paper addresses the mixing of hot jets in the lower plenum of the reactor core.

INL has developed a large Matched-Index-of-Refraction (MIR) flow system that uses optical techniques, such as laser Doppler velocimetry (LDV) and PIV, to obtain flow field measurements in complex passages without disturbing the flow. The refractive indices of the

fluid and the model are matched so that there is no optical distortion. The large size provides good spatial and temporal resolution and provides a means to measure flow fields, turbulence and mixing in the complex geometry of a prismatic VHTR lower plenum. The resulting data may be employed to validate CFD codes and their turbulence models for the limiting case of dominant forced convection where temperature can be considered to be a passive scalar. A code should be validated using this data before considering complicated phenomena (e.g., buoyancy influences).

The general approach of the overall project is to develop new benchmark experiments for validation in parallel with CFD and coupled CFD systems code calculations for the same geometry. The velocity and turbulence fields measured in the MIR flow system will be used to validate the capabilities of the CFD codes and their turbulence models and to provide guidance in improving the models. A model of the lower plenum based on a preliminary design provided by General Atomics, Inc. [4] was developed and employed in this experiment.

The *objective* of this paper is to *document the experiment and present a sample of the data set* that has been recorded and is offered as a benchmark experiment for flow phenomena expected to occur in the lower plenum of typical prismatic-core gas-cooled reactor.

## 3. SUMMARY OF PREVIOUS WORK

McEligot and McCreery [5] conducted scaling studies and conceptual designs for flow and heat-transfer experiments intended to assess CFD codes and their turbulence models proposed for application to prismatic VHTR concepts. Condie et al. [6] documented the design of the present experiment to measure generic flow phenomena expected to occur in the lower plenum of a typical prismatic VHTR. The product of these efforts resulted in the fabrication and installation of a scaled model of the region of a typical VHTR lower plenum that is near the outer reflector wall away from the plenum outlet.

## 4. APPARATUS SETUP

### 4.1. Matched-Index-of-Refraction (MIR) Flow Facility

Velocity field measurements were recorded in the MIR closed-loop flow system located at INL in Idaho Falls, Idaho (Fig. 1). Stoots et al. [7] presented a detailed review of this system. The system consists of a stainless steel closed flow loop with three polycarbonate and glass test sections. The facility can operate with water or light mineral oil as the working fluid. The working fluid for this experiment was light mineral oil that is circulated (clockwise in Fig. 1) by an axial pump powered by a 75-hp variable speed electric motor that can provide a maximum volumetric flow rate of approximately 0.6 $m^3/s$ of mineral oil through the test section. This maximum volumetric flow rate corresponds to a maximum test section inlet velocity of approximately 1.7 m/s. The test section includes three chambers that are constructed of 3.8 cm thick polycarbonate supported by a stainless steel framework. Each chamber is fitted with a removable lid. The test section inside dimension is 0.61 m square and is 2.44 m long. Both sides of each chamber of the test section are equipped with glass window inserts in the side panels to accommodate high quality measurements with LDV and/or PIV systems.

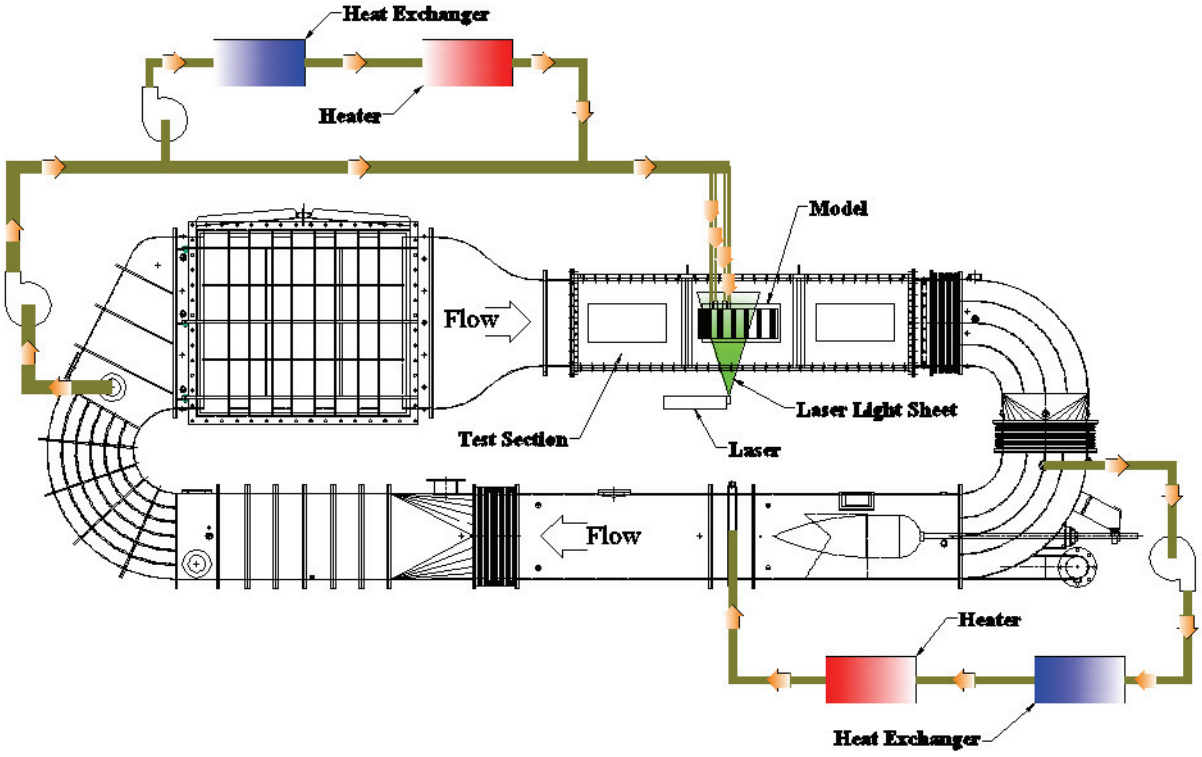


**Figure 1 MIR Facility.**

Mineral oil in the primary flow loop flows around the model for temperature control of the external surfaces of the model. The mineral oil temperature is maintained with a temperature control loop as shown in the lower right corner of Fig. 1. This loop extracts approximately 300 L/min of mineral oil from the primary flow loop which is pumped through a glycol-cooled heat exchanger and a 10 kW DC heater, filtered, and then re-injected into the primary flow loop. This temperature control system can maintain the fluid temperature in the test section to within ± 0.05 ºC of the specified index-matching temperature. An additional auxiliary flow loop (shown in the upper left corner of Fig. 1), with a similar temperature control system, is used to provide fluid for the inlet jets in the model. Fluid is extracted from the primary flow loop and routed to a seven horsepower auxiliary pump that produces flow to the model inlet jets. To maintain the required working fluid temperature, a portion of this fluid is extracted from the auxiliary loop and routed through a parallel auxiliary temperature control loop. As in the primary temperature control loop, the mineral oil is cooled and reheated before returning to the auxiliary flow loop and into the model inlet jets. Control instrumentation includes thermistors, flow meters, data acquisition, and computer controls.

### 4.2. Particle Image Velocimetry (PIV) System

Velocity field measurements were obtained with a 3-D PIV system from LaVision, Inc. The 3-D PIV system consists of two ImagerPro Plus digital charge coupled device (CCD) cameras and a double-pulsed Nd:YAG laser from Big Sky Laser. The system is controlled with DaVis 7.1 software. DaVis is a CCD image acquisition program developed by LaVision and controlled by a LaVision dual-processor Programmable Timing Unit (PTU). The PIV system cameras are mounted on a 3-directional traverse system that is controlled by three separate electric stepping motors. The cameras can be positioned and re-positioned to within 2 μm accuracy using linear stages and digital readouts at the operator's station. The spanwise laser position is also controlled with an electric stepping motor. The laser can be positioned to within 5 μm accuracy with an optical linear stage and digital readout that is also located at the operator's station. The PIV system laser was mounted below the experiment model (Fig. 1) and produced a vertical light sheet approximately 2 mm thick. Both of the two PIV system cameras were mounted on one side of the test section and aligned horizontally for camera views at right angles to the plane of the vertical light sheet.

### 4.3. Experimental Model

Fig. 2 is a picture of the experimental model that was installed in the MIR test section. The model is fabricated from fused quartz and carefully positioned, located and fixed in the test

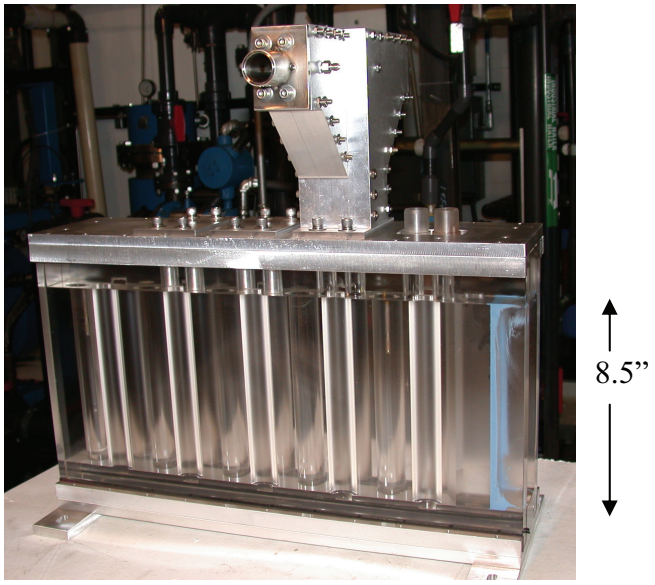


**Figure 2 Quartz Experimental Model.**

section (see Appendix A by Condie et al. [6] for detailed drawings of the model). Table 1 lists some of the key dimensions of the model. Mineral oil from the auxiliary loop enters into the

model jets on the top of the model via four inlet jet elbow manifolds like the aluminum manifold shown in Fig. 2. The four inlet jet flows merge in the lower plenum and flow toward the outlet end of the model where the flow exits and merges with the primary loop flow. The four jet inlet flows are conditioned in the elbow manifolds to meet flow characteristics expected to be present in the typical GCR cooling channels that the inlet jets are simulating. Key requirements for the inlet-jet flows are that they are moderately turbulent, uniform and contain negligible swirl. When the working fluids reach the inlet jet elbow manifolds the flows are turned and straightened, then pass through a honeycomb, through a screen, and finally through a turbulence generator to induce expected levels of turbulence before entering the jet inlet ducts.

**Table 1. Key Dimensions**

| | |
|---|---|
| Model length | 558.80 mm |
| Model height | 306.40 mm |
| Model width | 104.78 mm |
| Channel height | 217.50 mm |
| Channel width | 53.98 mm |
| Post diameter | 31.75 mm |
| Post height | 217.5 mm |
| Jet inlet diameter | 22.10 mm |
| Centerline distance between posts | 93.50 mm |
| Ratio of plenum height to post diameter | 6.85 |
| Ratio of jet diameter to post diameter | 0.7 |
| Ratio of channel width to post diameter | 1.7 |

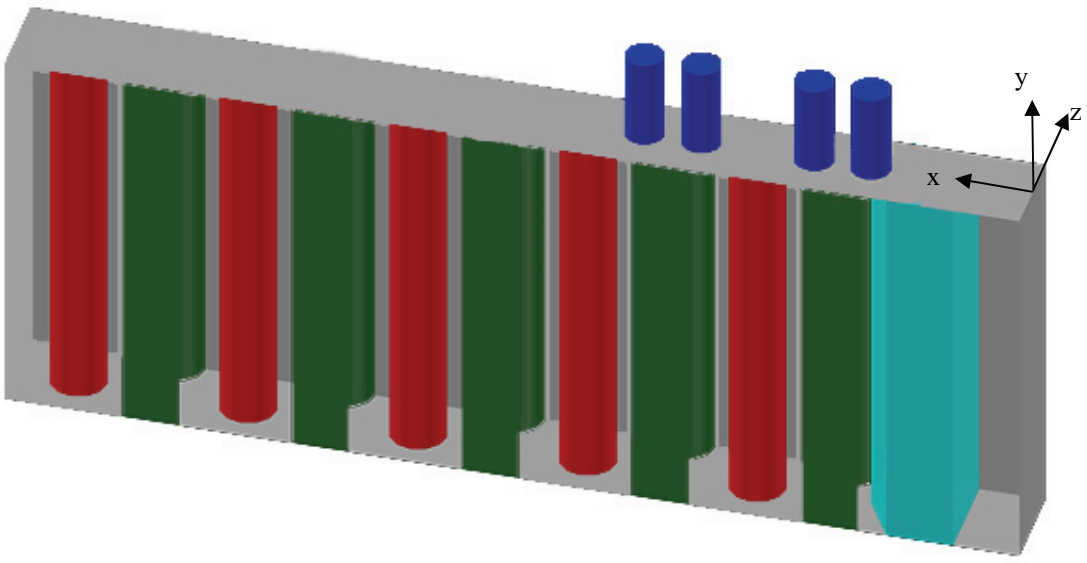


**Figure 3 Quartz Model and Axis Origin.**

Fig. 3 is a representation of the interior of the quartz model and shows the axis origin at the top, right corner of the model. The four inlet jets are shown in dark blue, the model wall reflector is shown in light blue, the full centerline posts are shown in red, and the wall half-posts are shown in green. The flow enters the lower plenum from the four blue jets, merges below the jets and ultimately flows toward the outlet on the left end of the model. The jets are numbered right-to-left from 1 to 4. The centerline posts are numbered right-to-left from 1 to 5.

## 5. EXPERIMENTAL PROCEDURES

### 5.1. Primary Flow Loop

The main circulating pump was operated at 50 rpm to circulate the mineral oil through the primary flow loop at approximately 0.2 m/s for temperature control. The temperatures of both the primary flow loop and auxiliary flow loop were controlled with LabVIEW™ software. The temperature control system maintained the oil temperature to within ± 0.05 °C of the calculated index-matching temperature (~23.3 ºC) in the model and to within ± 0.03 ºC of the index-matching temperature in the primary flow loop. The facility remained at a constant, steady state condition throughout the data collection periods. Temperature records for all data collection files are archived on the temperature control computer.

### 5.2. PIV System

The PIV system was operated in the 3-D, Expert User mode. Laser power, Q-Switch delays, and the time interval between frames of the double-image cameras (dt) were adjusted using the Interactive Mode in the DaVis 3-D PIV software.

In an effort to balance the requirement for high resolution data and to keep the size of data files within reasonable limits (for data processing and data storage considerations) the collection effort on the model was divided into eight flow regions. The lower plenum area of the model was divided into six regions (a two-row, three-column matrix of regions) and the inlet jet area was divided into two regions (one region for jets l and 2 and one region for jets 3 and 4). Additionally, in order to collect (3-D) data across the entire width of the model channel (spanwise) the laser and cameras were positioned at 23 different spanwise planes. The laser-light sheet was adjusted to a thickness of about 2 mm which allowed complete, continuous coverage of the model except for an area near the model walls where the laser-light sheet was blocked by O-ring seals. Therefore, each region of the lower plenum consisted of 23 PIV image files–one file for each spanwise plane. The inlet-jet regions only required 11 planes/files to cover the full width of the jets.

Because of the refractive index difference between the air space where the cameras operated and the mineral oil where the light sheet was located, it was necessary to coordinate the movement of the two digital cameras relative to the movement of the laser-light sheet. This coordination was accomplished with a MATHCAD code. The code used the mineral oil temperature to determine the index of refraction of the mineral oil and the camera angles relative to the laser-light sheet

reported by the camera calibration procedure to calculate a movement ratio for the camera movement relative to the laser light sheet movement. This ratio was typically between 0.62 and 0.68, that is, for a movement ratio of 0.66, a 2 mm shift of the laser-light sheet required the camera support to be moved about 1.32 mm.

Table 2 summarizes the settings used on the MIR and PIV systems.

**Table 2. MIR and PIV Settings**

| | $Re_{Jet}$ 4300 | $Re_{Jet}$ 12400 |
|---|---|---|
| **MIR** | | |
| Jet No. 1 Flow Rate (gallons per minute [gpm]) | 11.25 | 32.11 |
| Jet No. 2 Flow Rate (gpm) | 16.75 | 48.14 |
| Jet No. 3 Flow Rate (gpm) | 16.75 | 48.14 |
| Jet No. 4 Flow Rate (gpm) | 16.75 | 48.14 |
| **PIV** | | |
| **Camera Mode** | 3-D Cross Correlation | 3-D Cross Correlation |
| dt (time interval between image frames) | Various | Various |
| Laser Power | Various | Various |
| Q-Switch Delays @ Maximum Power (Laser 1/Laser 2) | 175/175 | Various |
| Q-Switch Delays @ Minimum Power (Laser 1/Laser 2) | 370/385 | Various |
| Image Acquisition Method | RAM (fast) | Standard |
| Acquisition – Number of Images | 170 | 750 |

### 5.3. Data Processing

Data post-processing of the acquired images was accomplished with DaVis 7.1 software. The post-processed data were then exported from DaVis to a secondary PC where data were organized and displayed with TecPlot and/or MS Excel software. The total processing time exceeded 900 hours of computer time and produced approximately 2 TB of data.

## 6. UNCERTAINTY ANALYSIS

The objective of uncertainty analyses is to estimate the experimental uncertainty of the data. For proper benchmark databases, the experimental uncertainties of all measured quantities and their propagation into the results must be obtained quantitatively. In a complicated experiment such as this, some experimental uncertainties can be expected to vary significantly with position as the local velocities vary. As a partial tabulation, estimated uncertainties that are expected to be required include: instantaneous and mean velocity components and their mean statistics, sample size, measurement positions relative to the model, seeding particle velocity, fluid properties and transient temperatures and pertinent instrument characteristics, model geometry, and flow rates.

### 6.1. Estimates of PIV Measuring Uncertainty

The basic measurement of a PIV system is an instantaneous velocity component $\left(V_p\right)$ deduced from the translation $\left(\Delta x_p\right)$ of a group of particles over a time interval $\left(\Delta t\right)$ so that

$$V_p = \frac{\left(\Delta x_p\right)}{\Delta t} \tag{1}$$

where the subscript ***p*** indicates a measurement in pixels of the recorded image. The per cent uncertainty in the velocity can be represented as

$$\left(\%Unc\, V_p\right) = \left[\left(\%Unc\, \Delta x_p\right)^2 + \left(\%Unc\, \Delta t\right)^2\right]^{1/2}. \tag{2}$$

The propagation of such uncertainties into the mean statistics then depends on the extent to which the uncertainties are random (precision) or systematic (bias) and the manner of presentation of results. In some situations fixed uncertainties can be removed from the presentation by normalizing the quantities involved. The averaging process for determining mean statistics will reduce the resulting per-cent uncertainties when they are random. The PIV manufacturer (LaVision) provides estimates of the accuracy of vectors for calculations done with their standard Fast Fourier Transform (FFT) correlation. With 20 particles in an interrogation area of 32 × 32 pixels, bias and root mean square (RMS) errors vary from about 0.025 to 0.1 pixels for displacements Δx of 1 to 10 pixels. With the interrogation area of 16 × 16 pixels and 200 particles, these uncertainties fall in a range of about 0.1 to 0.2 pixels up to Δx of seven, and then the uncertainties rapidly increase. By employing an adaptive multipass technique first with 64 × 64 pixels and then 32 × 32 pixels, bias and RMS errors are reduced to about 0.03 pixels for up to 10 pixel displacements. LaVision suggests that RMS-error is a function of the size of interrogation window, number of particles, local velocity gradients inside the interrogation window, non-matching particles, and noise, such that RMS-error (random uncertainty) in an individual realization is typically 0.05 to 0.1 pixels in real data.

LaVision also notes that a particle image diameter of less than one pixel can cause bias during vector calculation. They recommend a particle image diameter of at least two pixels. The processing algorithm for the LaVision PIV system gives uncertainties in displacements of about 0.05 pixels for synthetic images. For images of real experiments, additional factors involved include calibration, focus, displacement of particles, particle seeding, spatial gradients within each interrogation spot, image contrast, and operator settings, etc. Therefore, the value of 0.05 pixels can be considered reasonable under ideal circumstances.

For the LaVision PIV system, the random uncertainty in the timing is estimated to be about 1 nsec. For the typical pulse separation of 100 μsec (or more) used for the MIR PIV, the uncertainty would be about ≤0.001% and therefore negligible compared to the displacement uncertainty.

To convert the basic PIV observation to actual velocities, a scaling factor is employed relating the pixel dimensions to physical distance in the field of view. This quantity can suffer from both systematic (fixed) and random uncertainties. The physical distance can be provided from a calibration device, fabrication sketches with tolerances, as-built drawings, and/or independent measurements. The connection to the pixel grid is obtained via the camera view for the same location(s). In 3-D operation with two cameras, a LaVision calibration plate and related software are employed to relate the observed image dimensions in pixels to physical distances in the oil. From this determination, a scale factor is calculated in mm/pixel. Estimates of the uncertainties involved in this process are not available. Also, in 3-D operation, the laser sheet thickness may be determined from measuring a correlation peak once a self-calibration procedure is completed. The laser-light sheet thickness was estimated to be 2 ± 0.2 mm.

For this study, the total uncertainty (random and bias) in the mean velocity measurements for the low flow-rate case of $Re_{Jet}$ ~ 4300 ranges from approximately 0.5% to 1.2% and from approximately 0.3% to 1% for the higher-flow case of $Re_{Jet}$ ~12400. The total uncertainty in the turbulence intensity is approximately 1.8%.

### 6.2. Sample Size

Measurements of the flow field in the lower Reynolds-number experiments ($Re_{Jet}$ ~4300) were made with 170 image pairs per file. This procedure was adopted to capture the flow variations at the maximum frequency of the PIV system. This technique required that the images be stored in the LaVision PTU RAM, which limited each file to 170 images. The resulting data may have suffered from an insufficient number of independent realizations necessary to produce reasonable mean statistics. For this reason the measurement data from the lower Reynolds-number flow are considered to be preliminary.

For the higher Reynolds-number experiments ($Re_{Jet}$ ~12400), the effect of sample size for a typical set of measurements was examined using an approach comparable to that of Uzol and Camci [8]. Three thousand images of a region below a single inlet jet were collected. The region below an inlet jet was selected because it offered a wide range of velocity and turbulence intensity. The variations in mean statistics were evaluated at seven locations as the number of samples was varied from 100 to 1500. Mean velocities varied from about 9 m/s to 0.7 m/s for these seven positions and mean-squared fluctuations varied from about 0.05 $m^2/s^2$ to 4 $m^2/s^2$. About 10% of the vectors under the inlet jets and at the bottom of the plenum in the slower region failed to meet certain criteria established in the vector post-processing operation and were rejected, while in the middle of the plenum about thirty per cent or more of the vectors were rejected. The mean statistics calculated were based on the number of *valid* vectors at each point. Thus, for 1000 samples there would have been about 700 to 900 individual realizations, depending on the location.

This approach evaluates effects of random uncertainties on the mean statistics for this particular situation (image acquisition and data processing). Trends generally followed those observed by Uzol and Camci. Preliminary conclusions were that for this study about 750 images should be collected to reduce the scatter in mean-velocity statistics to between 0.4 and 10% of velocities greater than about 2 m/s.

Also, for this study of sample size, the time interval (dt) was 120 μs and the scaling factor was about 9.4 pixels/mm. Thus the estimate of random uncertainties in an independent realization is about 0.3 m/s, using an estimated displacement uncertainty of 0.3 pixels. Mean velocities varied from about 9 m/s in the jet to 0.7 m/s in the middle of the plenum. Corresponding instantaneous uncertainties were about 3 and 40%, respectively. For 1000 samples, these values were about 0.1 and 2%. The former is consistent with the scatter observed in the sampling study but the latter is about an order-of-magnitude less. Approximate levels of mean-square-fluctuations were 0.05 $m^2/s^2$ and 1.5 $m^2/s^2$ for these two extremes (giving turbulence intensity over 100% in the second case). The resulting random uncertainties predicted are then 0.003 $m^2/s^2$ and 0.02 $m^2/s^2$, respectively. Both of these values are less than the scatter observed in the data processing.

The trends predicted by this uncertainty analysis are consistent with observations but, for the most part, the expected values are less than the scatter observed. Possible explanations are that the displacement uncertainty has been underestimated, that a periodic process such as eddy shedding is affecting the results, and/or some other unknown reason(s). Preliminary conclusions from the comparison were that more samples should be collected than predicted by a traditional uncertainty analysis, and the time intervals (dt) should be evaluated and adjusted for the specific conditions of each collection region.

### 6.3. Positioning Uncertainty

A three-directional traversing mechanism was used to avoid relative motion between the test section and the optics. This traverse system supports the two digital CCD cameras and can measure model locations in conjunction with a PIV camera and its cursor. For all directional motions, platforms are moved under precise computer control to maintain alignment. Positioning is computer-controlled and determined with digital readouts, with estimated uncertainties of about ± 2.5 μm. The readout displays movement increments of 2 μm.

For measurements in the vertical plane of the light sheet (i.e., x and y), the origin of the model coordinate system is taken at the upstream end of the model on the vertical-center plane where it intersects the top of the model flow passage (Fig. 3). To determine locations within the image views, secondary reference points were established. For this purpose, holes were bored vertically in two central quartz posts on their centerlines; pointed metal rods were installed in these holes to provide known reference points (within their fabrication tolerances). For views that do not include one of these reference positions, a reference is established at an intersection between the vertical-center plane and the upstream (or downstream) face of a central post where it meets the bottom of the upper quartz block or the top of the lower block. (Because the oil temperature is adjusted to match refractive indices at 532 nm, it is possible to see quartz-oil interfaces in the camera view at other wave lengths in the visible spectrum.)

The estimated uncertainty in absolute location of a reference point in model coordinates depends on the propagation of fabrication tolerances for reference point locations, reference-point hole diameters, and diameters of the ends of the reference posts. For the current experiment, it is estimated that a point in an image may be determined to within about 0.11 mm by using the cursor and image magnification. Thus, a relative location between two points within the same

image view may be determined to about $(2)^{1/2}$ x 0.11 ≈ 0.16 mm. The DaVis software also has a measuring tool that is calibrated to model dimensions during the calibration procedure. This measuring tool may be employed to determine distances between two points in a view, but currently we do not have estimates of its experimental uncertainties.

During experiments, the x, y, and z locations of the camera traverse, and the z location of the laser-light sheet are recorded for every file. Additionally, the position of the laser light sheet is controlled by a stepping motor and linear stage with digital readout. The laser head is mounted on a linear stage that is positioned under the test section. The streamwise position of the laser head is made by hand (a non-critical position), but the spanwise position of the laser head (and laser light sheet) is controlled by the stepping motor. The estimated linear-stage and digital-readout uncertainties are about ±5 μm.

### 6.4. Seeding Particle Settling Velocity

Our approach to examine the question of particle motion relative to fluid motion, i.e., to what extent the measured particle velocities represent the desired fluid velocities, is in terms of settling velocity or terminal velocity due to gravity. The terminal velocity for a small particle falling through a stagnant fluid due to gravitational forces can be estimated via a force balance for steady motion,

$$\frac{dV}{dt} = 0 = \left(\frac{4}{3}\right)\pi a^3 \left(\rho_p - \rho_f\right) - 6\pi\mu a\phi V \qquad (3)$$

where $a$ is the particle diameter, $\rho_p$ is the particle density, $\rho_f$ is the fluid density, $\mu$ is the fluid viscosity, and $V$ is the settling velocity. The first term is the difference between the gravitational force and buoyancy while the second represents drag on the particle. The quantity, $\phi$, is a correction factor relative to Stokes drag; it approaches unity as the particle Reynolds number approaches zero. This relation can be rearranged to yield the settling velocity as

$$V \approx \left(\frac{2ag}{9\phi}\right)\left[\left(\frac{\rho_p}{\rho_f}\right) - 1\right] \qquad (4)$$

For our particles of about 1.7 g/cc and radii of 10 μm, this estimate gives about 0.02 mm/s or less and $Re_p \approx 3 \times 10^{-5}$. The lowest flow velocity we might encounter is about 1 cm/s. Thus, the particles are expected to follow the flow adequately.

### 6.5. Fluid Properties

During this experiment the oil temperature is routinely maintained at 23.3 ºC ± 0.03ºC for the main test section (main flow) and 23.3 ºC ± 0.05ºC for the flow into the model; these variations contribute to random uncertainties in measurement series. The related bias uncertainties are about 0.2%, 2%, and 0.02% for the calibrations of density (ρ), kinematic viscosity (ν), and the refractive index (n), respectively. The random uncertainty in kinematic viscosity due to

temperature fluctuations of 0.05ºC would be 0.2%.

### 6.6. Geometry

As-built measurements of model components have demonstrated that the resulting dimensions are within the tolerances specified in the fabrication sketches. For the key internal dimensions these tolerances are ± 0.05 mm with the exception of the post heights, which are ± 0.13 mm. The diameters of the jet inlet ducts are specified as 22.1 ± 0.05 mm for bias uncertainties of about 0.2%.

### 6.7. Flow Rates

Flow is provided to the four inlet jets from the top of the model. The flow rates to the jets were measured individually with four variable-area flow meters from Flowmetrics, Inc. The flow meters have stainless steel floats. The flow meters were calibrated for our approximate operating conditions to within 0.5% of reading, for an effective flow range of 2.5 to 60 gpm of mineral oil. This uncertainty can be considered to be a bias uncertainty. Typical minimum flow rates (for jet flows at $Re_{Jet}$ ~4300) are about 11 gpm so the float level can be expected to be 18% to 20% of full scale. The principle of operation of the flow meter is that the float configuration forms a sharp-edged annular orifice with the surrounding circular tube with its differential pressure force balancing the effective weight of the float. A force balance, in terms of the orifice loss coefficient (which is a function of level) can be derived to provide a relation between the velocity through the orifice and the liquid density; the geometric quantities are fixed at a given level. This relation can be rearranged to permit measurement with a fluid of one density after calibration with a fluid of another density. The loss coefficient is relatively independent of the Reynolds number, except at low-flow rates. The manufacturer indicates that for this model the "viscosity immunity ceiling" is 46 cp at a fluid-specific gravity of 1.00 or, effectively, 14 cS. The conversion from one fluid to another will involve bias uncertainties due to uncertainties in the densities and, during experiment operation, random uncertainties from the effects of temperature variation on the density of the operating fluid. Uncertainties in reading the flow rates from the meters would be random uncertainties of about one-quarter to one-half division. The present meters have two scales. The glass tubes are scribed in millimeters from zero to the maximum of 600 mm. A separate scale provides the calibration for oil (at 100ºF to give a kinematic viscosity of 14 cS) in intervals of 0.25 gpm from 1.75 to 60 gpm. The calibrated scale was used for setting and measuring the flow rate. The specified oil density of the calibration is 0.83 g/mL, implying an uncertainty of 0.005 g/mL. This uncertainty converts to a bias uncertainty in measured flow rate of about 0.34%. Our target oil temperature of 23.3ºC gives an oil density of 0.8312 g/mL which is well within the range of uncertainty of the calibration density. Uncertainties in reproducing the specified flow rates of an experiment depend on the manner in which these flow rates are set. It is estimated that the flow rate settings can be repeated to within about 0.125 gpm for each jet. The lowest flow rates of the $Re_{Jet}$ ~4300 experiments are typically 11.2 gpm (float height about 91.3 mm) for the first jet, which has a smaller cross section than the rest, and 16.7 gpm (about 148.7 mm) for the other three. Because the total volume flow rate $\left(Q_{Total}\right)$ is obtained by adding the flow rates from the individual jets operating, the absolute random uncertainty of the total is given by the absolute uncertainties of the number of jets operating as

$$\delta Q_{Total} \approx \left[N_{Jets}\right]^{1/2} \delta Q_{Jet} \tag{5}$$

because their random uncertainties are the same. At 11.2 gpm the bias uncertainty would be 0.5% or about 0.06 gpm, and the random uncertainty can be taken as 0.125 gpm or about 1%. For the jets at 16.7 gpm the bias uncertainty would be about 0.08 gpm (~0.5%) and the random uncertainty would again be 0.125 gpm (~0.7%).

For the total flow rate, the per cent uncertainties would be about 0.4 and 0.6% for the bias and random uncertainties, respectively. At higher flow rates the bias uncertainties would become larger than the random uncertainty.

### 6.8. Reynolds Numbers

The inlet jet Reynolds number is defined as

$$\mathrm{Re}_{Jet} = \frac{V_b\, d_{Jet}}{\nu} \tag{6}$$

where $V_b$ is the bulk velocity, $d_{Jet}$ is the jet inlet diameter, and $\nu$ is the kinematic viscosity of mineral oil. This expression can be converted to

$$\mathrm{Re}_{Jet} = \frac{4\dot{m}_{Jet}}{\pi\, d_{Jet}\, \mu} = \frac{4 Q_{Jet}}{\pi\, d_{Jet}\, \nu} \tag{7}$$

where $\dot{m}_{Jet}$ is the mass flow rate of fluid through the jet and $\mu$ is the absolute viscosity of mineral oil. Therefore, the percent uncertainty in $\mathrm{Re}_{Jet}$ can be estimated from the RMS sum of the per cent uncertainties of these variables, which for a single jet would be

$$\frac{\delta \mathrm{Re}_{Jet}}{\mathrm{Re}_{Jet}} \approx \left[\left(\frac{\delta Q_{Jet}}{Q_{Jet}}\right)^2 + \left(\frac{\delta d_{Jet}}{d_{Jet}}\right)^2 + \left(\frac{\delta \nu}{\nu}\right)^2\right]^{1/2}. \tag{8}$$

At a flow rate of 11.2 gpm, the bias uncertainty would be

$$\frac{\delta \mathrm{Re}_{Jet}}{\mathrm{Re}_{Jet}} \approx \left[(0.005)^2 + (0.0023)^2 + (0.0213)^2\right]^{1/2} \approx 0.022 \approx 2\%, \tag{9}$$

and the random uncertainty would be

$$\frac{\delta \mathrm{Re}_{Jet}}{\mathrm{Re}_{Jet}} \approx \left[(0.011)^2 + (0.0023)^2\right]^{1/2} \approx 0.011 \approx 1\%. \tag{10}$$

The bias uncertainty is dominated by the uncertainty in the calibration of viscosity (v) and is relatively independent of the other two uncertainties. The per-cent-random uncertainty will

decrease as the flow rate increases.

## 7. EXPERIMENTAL RESULTS

The objective of the experimental program was to obtain velocity field measurements for CFD code validation. To accomplish this objective the flow inside the lower plenum model was characterized with velocity-vector fields and fourteen scalar quantities. Table 2 lists the vector field and scalars that were obtained. These LaVision symbols appear in some of the following figures.

**Table 2. Measurements**

| Field Measurement | LaVision Symbol | Remarks |
|---|---|---|
| **Vector field** | Avg V | Calculated time-mean average resultant (3-D) vector magnitudes for the number of images/vector fields collected and processed |
| **Scalar field** | Avg Vx<br>Avg Vy<br>Avg Vz | Calculated scalar values of the time-mean average velocity of each vector component for the number of vector fields collected and processed |
| **Scalar field** | RMS Vx<br>RMS Vy<br>RMS Vz | Calculated scalar values of the root-mean-squared fluctuations in the velocity of each vector component for the number of vector fields collected and processed |
| **Scalar field** | RE xy<br>RE xz<br>RE yz<br>RE xx<br>RE yy<br>RE zz | Calculated scalar values of the time-mean average Reynolds stresses (RE) for the number of vector fields collected and processed |
| **Scalar field** | Avg KE | Calculated scalar values of the time-mean average kinetic energy (KE) of the mean velocity field based on time-mean average velocities for the number of vector fields collected and processed |
| **Scalar field** | Turb KE | Calculated scalar values of the time-mean average turbulent kinetic energy based on the time-mean average velocity fluctuations for the number of vector fields collected and processed |

Since uniform time intervals were employed, the time-mean statistics are calculated from suitable arithmetic averages of the stored data.

### 7.1. Data Samples

The principle objective of this effort is to document the experiment and the data set. The data set presented here is a sample of the data available for code validation. Due to the tremendous

volume of data obtained and the complicated nature of the flow, only a brief analysis is presented. Therefore, this paper will present data at specific locations in the lower plenum and describe some of the major phenomena observed in the flow.

Figs. 4 and 5 are mean streamline plots from the DaVis PIV software of the flow along the centerline of the model from the model reflector wall (on right side of the model) to the upstream side of the fourth centerline support post. The diagram at the top of Fig. 4 shows the location of

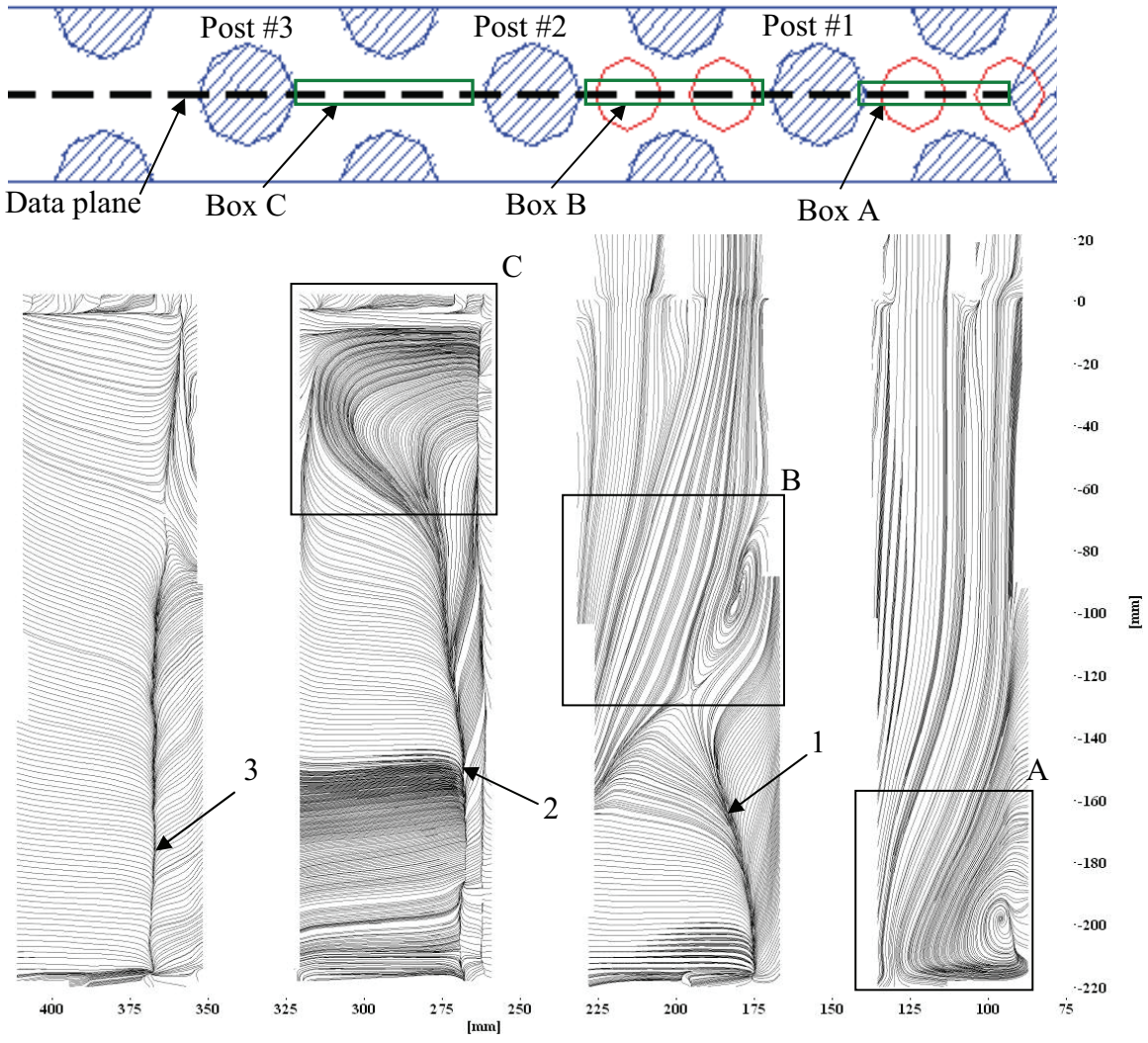


**Figure 4 Mean Streamlines for $Re_{Jet} \sim 4300$**

the data plane and a top view of the lettered box locations. The blank regions between the streamlines represent the support posts. Flow enters the model vertically from the four inlet jets located at the top-right corner of the picture (red circles in top diagram) and streams downward into the lower plenum where it interacts with the support posts and reflector wall, and then turns

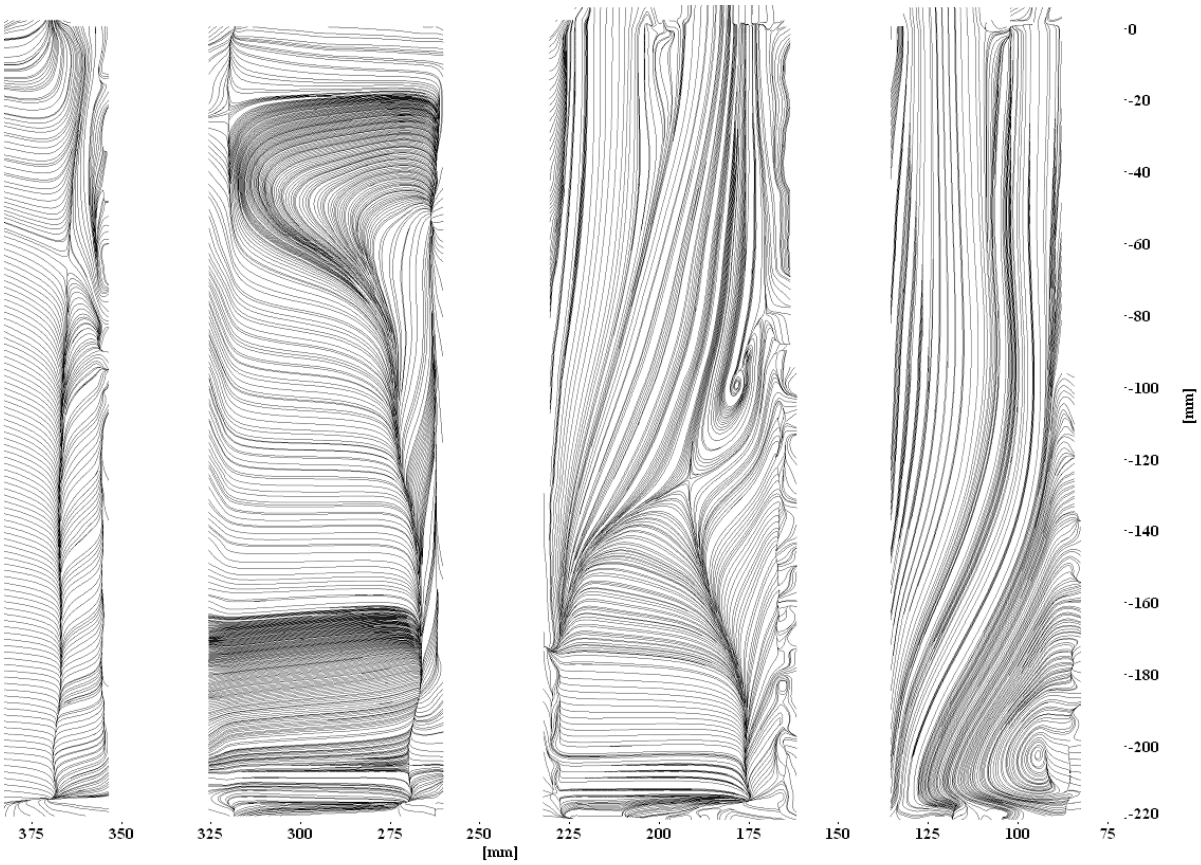


**Figure 5 Mean Streamlines for $Re_{Jet}$ ~12400.**

toward the left and flows toward the model exit located to the left of the picture. Fig. 4 shows the mean streamlines for the flow with an inlet-jet Reynolds number ($Re_{Jet}$) of ~4300 (based on the inlet jet diameter), and Fig. 5 shows the mean streamlines for the flow with $Re_{Jet}$ of ~12400. Three major recirculation zones are clearly visible in Fig. 4 (indicated by the lettered squares): the recirculation zone in the lower right corner (A), the recirculation zone near the mid-height of the model between the first two support posts (B), and the recirculation zone near the top of the model on the downstream side of the second and third support posts (C). Three secondary zones of merging flow are also visible (indicated by the three numbered arrows): the line of merging flow below the downstream (left) pair of jets and just downstream of the first support post from the bottom of the model to just below the recirculation zone (1), the line of merging flow just downstream of the second support post that extends about two-thirds of the distance from the bottom to the top of the model (2), and the line of merging flow that extends along the full channel height on the downstream side of the third support post (3). Fig. 6 is a vector plot of the $Re_{Jet}$ ~4300 flow that describes both directions and magnitudes of the flow.

The first major the recirculation zone is in the lower right corner of Fig. 4 (box A). This recirculation zone is formed by the first pair of inlet jets and their interaction with the reflector wall, first support post, and the bottom of the model. The flows from the two jets merge quickly

near the top of the model and are channeled downward between the first support post and reflector wall. As the flow approaches the bottom the major portion of this flow turns to the left, flows around the first support post, and interacts with the flow from the second pair of jets. A small portion of this flow is forced to the right where it encounters the reflector wall and creates a recirculation zone. Some of this recirculating fluid is forced up the reflector wall where it interacts with the downward flow from the jets and is subsequently reversed and forced toward the bottom of model plenum.

The second major recirculation zone is formed by the flow from the second pair of jets (box B). These flows also merge near the top of the plenum and are channeled downward in the area between the first and second support posts where they interact with the flow from the first (upstream) pair of jets that has moved around the first support post. This interaction results in a portion of the flow rising up the downstream edge of the first support post, causing a second recirculation zone about half way up the downstream edge of the first support post. The remainder of the flow generates a wake behind the lower portion of the second support post and then begins to flow toward the model exit (toward the left).

The third major recirculation zones is formed as the flows from both jet pairs merge and begin to flow toward the exit and interact with the second support post (box C). Because no fluid is entering the plenum downstream of the second support post (no inlet jets above this region corresponds to the central section of an annular core/plenum), the fluid flows around the second post, forms a wake and begins to rise to fill the upper portion of the model. A portion of this flow

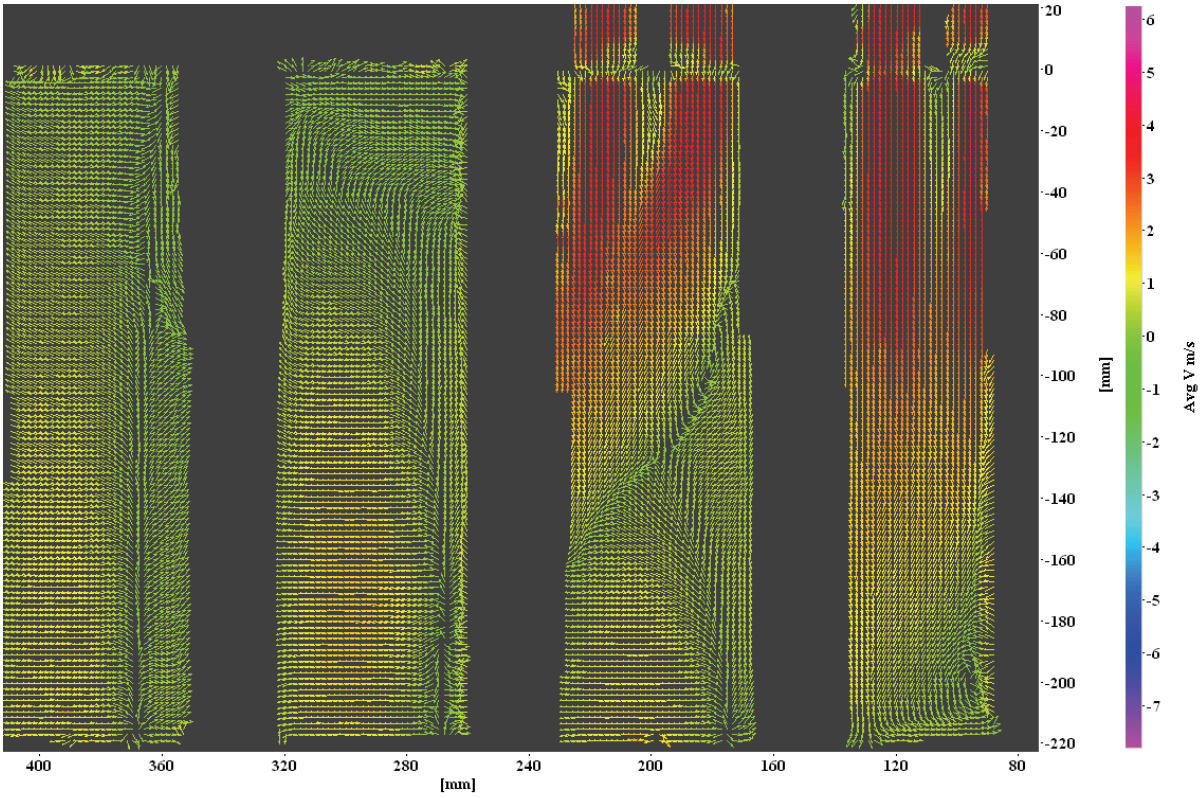


**Figure 6 Mean Vector Field for $Re_{Jet}$ ~4300.**

near the top of the plenum is pushed to the right on the downstream side of the second support post, and then downward forming the third recirculation zone. The flows in the bottom half of the model on the downstream side of the second support post merge and are pushed toward the model exit by the upstream fluid. This fluid then moves around the third support post, merges in a wake on the downstream side of the post, and gradually flows toward the left and slightly upward as it moves toward the model exit.

Fig. 7 is a vector plot of a small recirculation zone on the downstream side of the third support post. This flow appears to be a result of the recirculating flow on the upstream side of the post. On the downstream side of the post the upper portion of the flow is moving downward until it joins the flow moving upward from the bottom of the model. These two flows merge and are pushed around the post where they join the recirculation zone between the second and third posts.

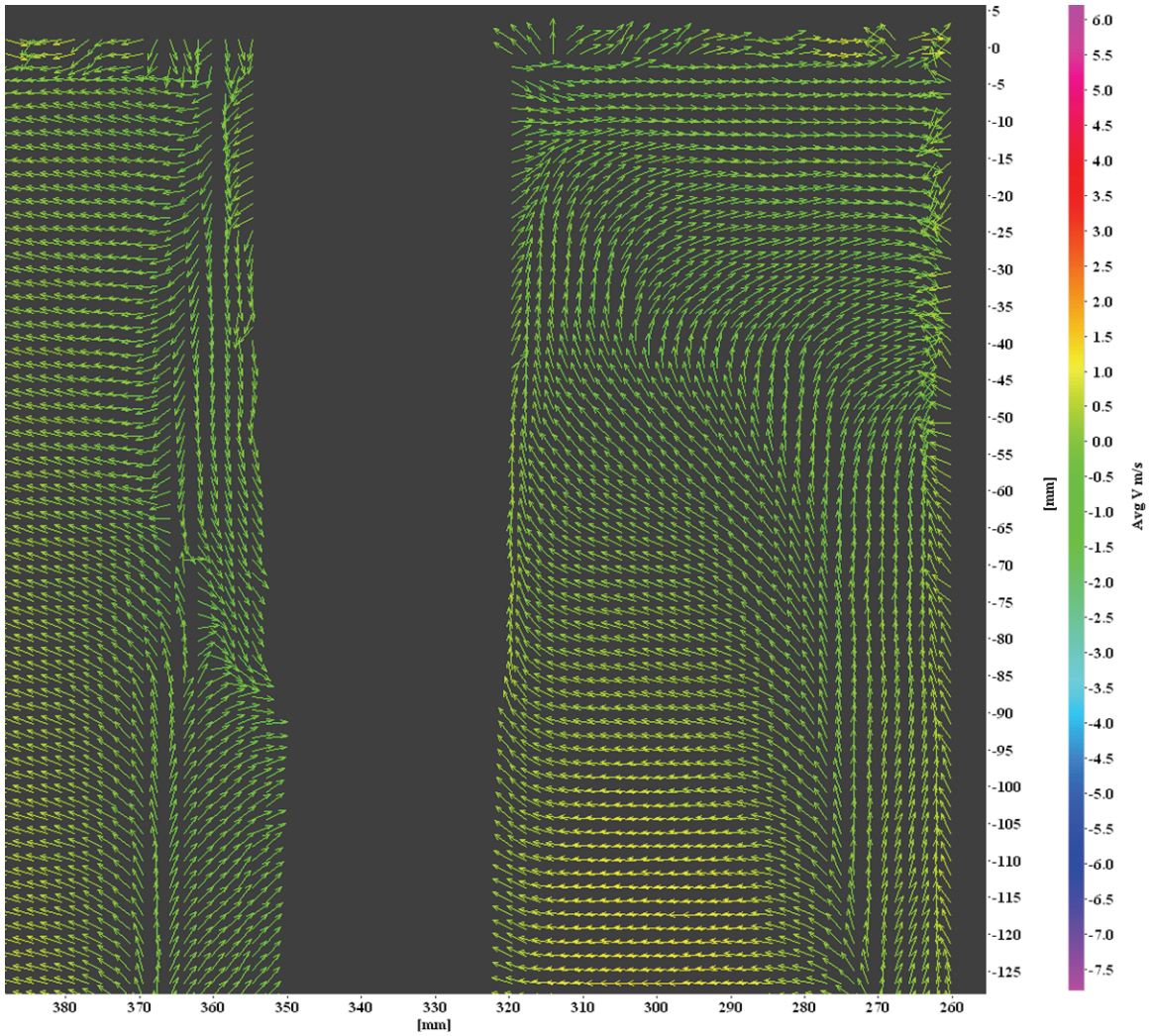


**Figure 7 Recirculation Zone Downstream of Post No. 3.**

The flow phenomena in the higher flow case ($Re_{Jet}$ ~12400) shown in Fig. 5 appear to be similar to that described above except for minor changes in the location of the structures. In this higher flow case the recirculation zone near the bottom right corner of the image appears to have moved slightly downward and toward the reflector wall (right). Similarly, the recirculation zone downstream of the first support post appears to have moved slightly closer to the support post. Also, the large recirculation zone downstream of the second support post appears to be slightly larger and fills more of the area between the second and third support post. Additionally, while the wakes behind the second and third support posts appear to have moved slightly upstream, the wake behind the first support post appears to have moved slightly downstream, possibly due to the higher flow rates. Finally, the small recirculation zone on the downstream side of the third support post appears to be slightly larger and slightly higher than the recirculation zone in the lower flow case.

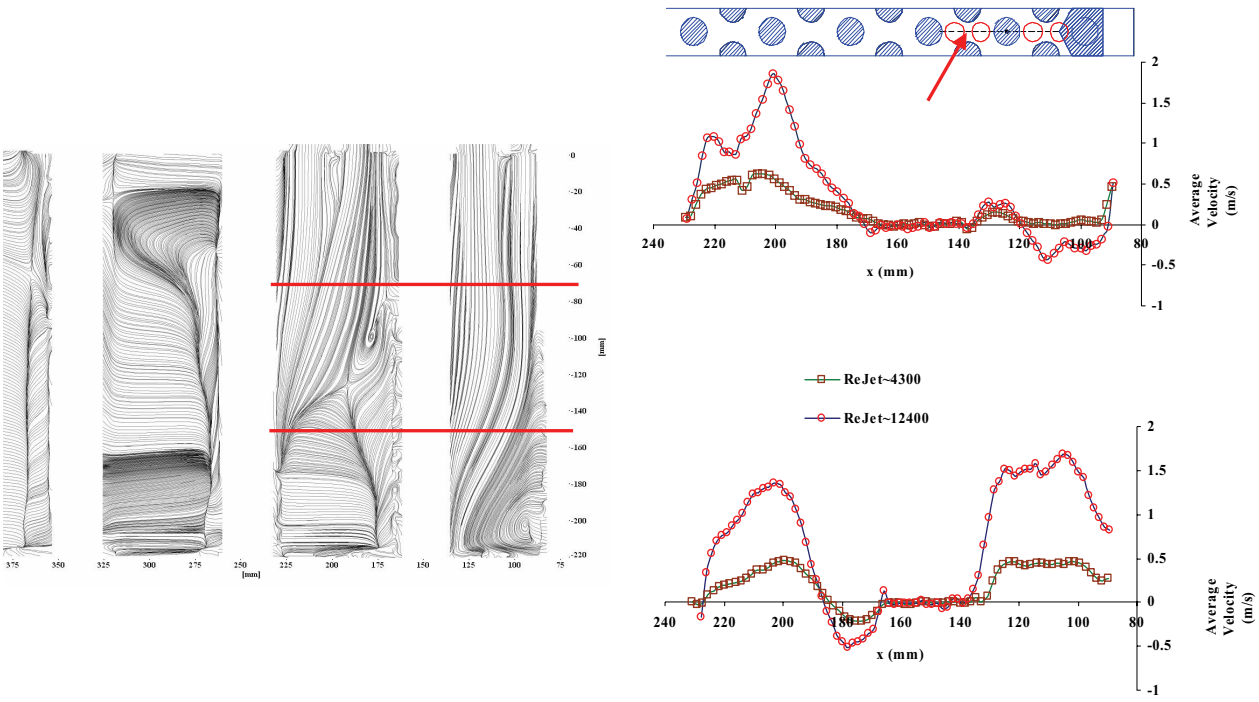


**Figure 8 Average Vx at y ~ -70 mm (top) and y ~ -150 mm (bottom).**

Fig. 8 displays values of mean Vx (streamwise velocity component) along a line from a vertical data slice along the centerline of the model in the regions below the inlet jets. The small diagram on top of the figure describes the spanwise location of the data slice, and the picture next to the charts shows the vertical locations of the data. The y~-70 mm data corresponds to the top red line in this picture, and the y~-150 mm data to the bottom red line. At the y~-70 mm depth, the

horizontal velocity is very small under jets 1 and 2 (primarily vertical momentum with no imposed crossflow), with some of the flow reversal observed in the streamline charts evident in the negative velocities (flow toward the right) under jets 1 and 2 (x ~ 90 mm to ~ 130 mm). Lower in the plenum (at y~-150 mm), the flow is mostly downstream toward the left except for a small area of negative flow (reversed flow toward the right) in the wake region downstream of the first support post (x ~ 170 mm to ~ 190 mm).

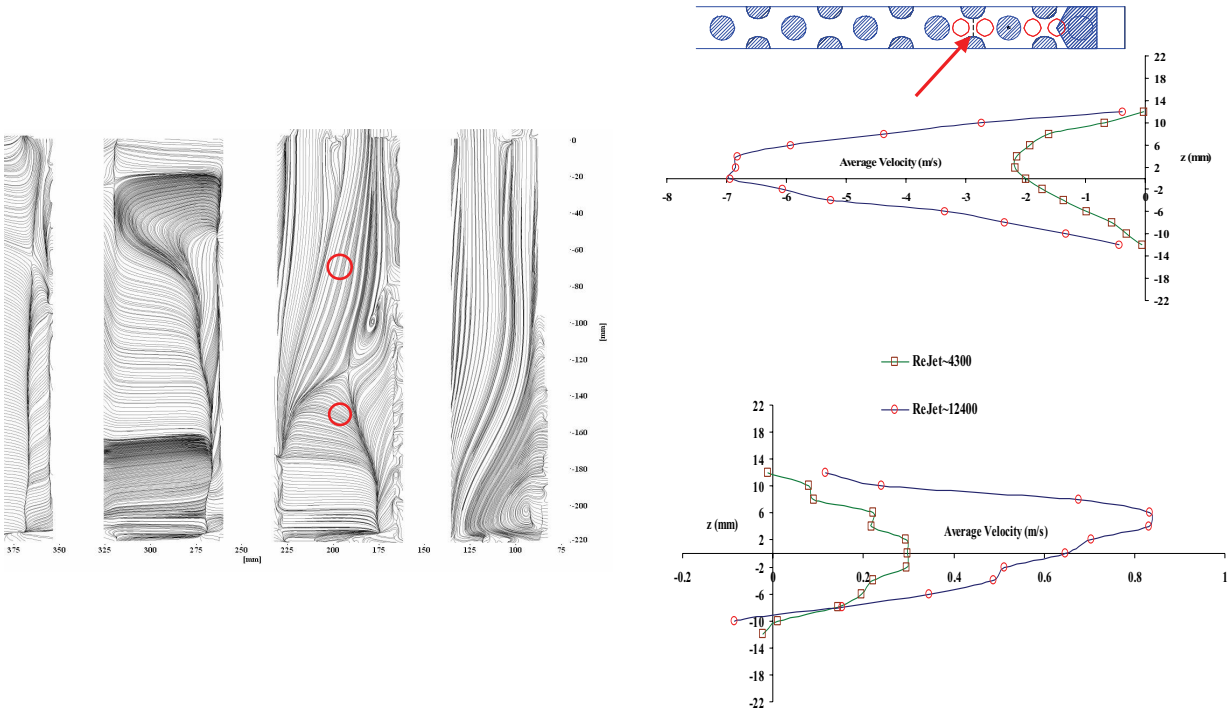


**Figure 9 Average Vy at y ~ -70 mm (top) and y ~ -150 mm (bottom).**

Fig. 9 displays values of mean Vy (vertical velocity component) in a spanwise line from a vertical data slice of the plenum between the half-posts between jets 3 and 4. The small diagram on top of the figure describes the location of the data slice, and the picture next to the charts shows the vertical locations of the data. The y ~ -70 mm data is at the center of the top red circle in this picture, and the y ~ -150 mm data are at the center of the bottom red circle. At y ~ -70 mm depth, the vertical velocity is substantial and negative (downward) from the inlet-jet flows entering the lower plenum from jets 3 and 4. Lower in the plenum (at y ~ -150), the vertical flow has reversed and is moving upward to form the bottom of a recirculation zone noted above (box B in Fig. 4).

Fig. 10 displays mean turbulence intensities for the same data slice as shown in Fig. 9. Because all three components of the velocity were measured, the turbulence intensity is defined by the relationship offered by Volino and Simon [9]

$$TI = \sqrt{\frac{\left(\overline{u'^2} + \overline{v'^2} + \overline{z'^2}\right)}{3 \cdot U_\infty^2}} \tag{11}$$

where $\sqrt{\overline{u'^2}}$ are the average RMS fluctuations in the horizontal velocity, Vx; $\sqrt{\overline{v'^2}}$ are the RMS fluctuations in vertical velocity, Vy; and $\sqrt{\overline{z'^2}}$ are the RMS fluctuations in the spanwise velocity, Vz; and $U_\infty$ is the maximum velocity reported for the data slice being investigated. As shown in Fig. 10, the normalized turbulence intensity apparently is larger for the lower Reynolds number flow.

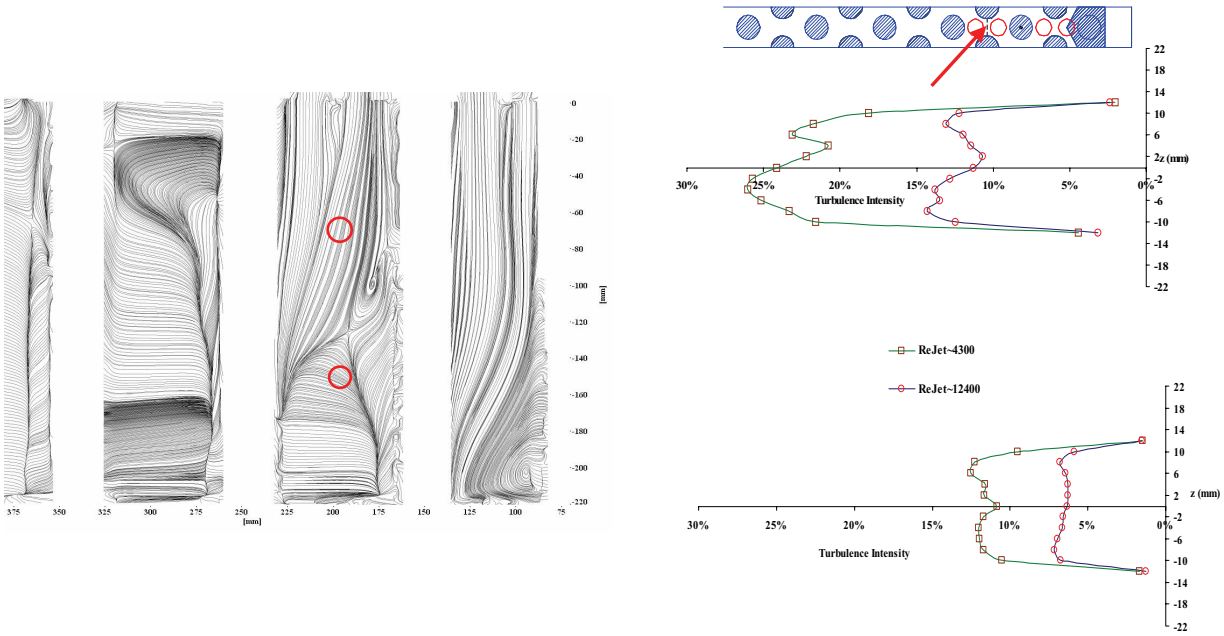


**Figure 10 Turbulence Intensity at y ~ -70 mm (top) and y ~ -150 mm (bottom).**

## 8. STANDARD PROBLEM

CFD analyses will be a major component in the analysis suite that will be needed to understand the internal flow behaviior and thus enable the plant operators to confidently all the reactor to operate at maximum outlet temperatures and efficiencies. Only CFD analysis tools have the capability to determine where localized hot spots will occur in the reactor and also whether or not unacceptably large thermal gradients are present.

The calculational envelope of the CFD tools used to analyze the behavior of the VHTR is defined by the scenarios and phenomena that these tools can calculate with confidence. CFD tools can only be used confidently when the results they produce have been shown to be in reasonable agreement with first-principle results, thought-problems, and data that describe the "highly ranked" phenomena inherent in all operational conditions and important accident scenarios for the VHTR. Reasonable agreement is achieved when the calculation generally lies within the uncertainty band of the data used for validation and always shows the same trends as the data and when code deficiencies are minor.

Presently, the CFD tools to be used for analyzing the VHTR are not ready to perform design and analysis, nor are they ready for licensing calculations to the standard that will be required by the VHTR. Considerable validation, and perhaps development of the software tools, is required. Additionally, practices and procedures are required for both validating and developing the necessary CFD software that are acceptable to the nuclear community.

The validation process is based on developing a set of standard problems that will populate a validation matrix for the various tools. The standard problems are defined by the Generation IV International Forum Standard Problem Committee, which defines its standard problems on the basis of comprehensive phenomena identification and ranking tables (PIRT) [10]. The standard problems, which are defined using high-quality data sets with known uncertainty bands, are the measures used to determine whether or not an analysis tool is capable of calculating the required phenomena. The members of the Standard Problem Committee are experts in the potential scenarios that are projected to be important in the VHTR.

The standard problems are passed to the Problem Oversight Committee. Members of this committee are experts in using and validating the analysis tools. Some members of this committee were specifically chosen due to their expertise in other industries where CFD is widely used. This committee defines the practices and procedures that must be used to perform the standard problems, and they also distribute the standard problem to the participants. Finally, the Problem Oversight Committee is responsible for coordinating the comparisons between the participants' solutions and the experimental results, including the evaluation of the validation. It is understood that many of the standard problem's calculations will be "blind," that is the participants will not be privy to the experimental data while their calculation is in progress.

Standard problems form the basis for determining whether a software tool is capable of analyzing the behavior of a reactor system undergoing a review for an operating license. The term "standard problem" stems from the use of the data sets that make up these problems as a measure (hence, a standard) to determine the acceptability of the software.

Standard problems consist of data sets that have the following characteristics:

a. The data set describes a phenomenon, or a set of phenomenon, that influences the behavior of an important figure-of-merit. That is, given that the figure-of-merit is the reactor vessel wall temperature, which must be less than a predetermined value, then important phenomena influence the reactor vessel wall temperature. Such phenomena are identified in

phenomena identification and ranking studies and are documented [10]. An example of such a phenomenon is the turbulent mixing of hot exit gases in the lower plenum of the reactor vessel because hot jets with an above-average temperature may impinge on the outlet plenum wall and perhaps cause a local hot spot on the reactor-vessel wall.

b. A phenomenon given in the standard problem data set, although it may be measured in a reduced-scale system, can be scaled to the full-sized system using accepted scaling practices. The scaling studies that link the experimental apparatus and data to the full-sized system are documented in reports.

c. The standard problem data set has been shown to measure the data required to determine whether the software are capable of calculating the important phenomenon.

d. The standard problem data set has estimated uncertainties associated with each data point.

e. The quality assurance procedures used to design the experiment, build the experiment, and conduct the experiment are consistent with NQA-1 requirements.

The experiment and results summarized in this paper are intended to validate CFD software; the MIR experiment meets the requirements just identified as items a – e above.

## 9. CONCLUDING REMARKS

The model and flow facility produced satisfactory flow conditions, as required by previous scaling studies and model design. As a result of the experiments described in this paper, the objectives of developing benchmark databases for the validation of CFD solutions of the momentum equations, scalar mixing and turbulence models for typical prismatic VHTR plenum geometries in the limiting case of negligible buoyancy and constant fluid properties have been met. Additionally, the data obtained from these experiments meet the requirements of a standard problem as defined.

Preliminary measurements of velocity components have been compiled for a low-power case of $Re_{Jet} \sim 4300$, and detailed measurements of the flow field for the maximum achievable flow rate in the present MIR Flow facility of $Re_{Jet} \sim 12400$ have also been completed. The data have been documented to identify and report estimated uncertainties of the measurements and have been collected into various formats suitable for release to the CFD community and others, as necessary. Future plans include distribution of instructions to obtain data sets and points of contact at INL.

## ACKNOWLEDGMENTS

The work was supported by the U. S. Department of Energy, Office of Nuclear Energy, Science and Technology (DOE-NE), under award DE-FC07-05ID14670 and DOE-NE Idaho Operations Office Contract DE-AC07-05ID14517. The authors also acknowledge the highly professional and timely support and assistance of Dr. Steven L. Anderson of LaVision, Inc., Professor Barton

L. Smith of Utah State University, and Richard R. Schultz of INL for their assistance in this project.

## REFERENCES

1. D. P. Mikielewicz, A. M. Shehata, J. D. Jackson and D. M. McEligot, "Temperature, Velocity and Mean Turbulence Structure in Strongly-Heated Internal Gas Flows. Comparison of Numerical Predictions with Data," *Int. J. Heat Mass Transfer*, **45**, pp. 4333-4352 (2002).
2. A. H. Richards, R. E. Spall and D. M. McEligot, "An Assessment of Turbulence Models for Strongly Heated Internal Gas Flows," *Proceedings of the Fifteenth IASTED International Conference on Modeling and Simulation Conference*, Marina Del Ray, CA., 1-3 March 2004, pp. 119-124 (2004).
3 . D. M. McEligot and twelve others, "Advanced Computational Thermal Physics (CTFP) and its Assessment for Light Water Reactors and Supercritical Reactors," *INEEL Technical Report INEEL/EXT-03-01215*, (2003).
4. P. E. MacDonald, J. W. Sterbentz, R. L. Sant, P. D. Bayless, R. R. Schultz, H. D. Gougar, R. L. Moore, A. M. Ougouag and W. K. Terry, "NGNP Preliminary Point Design – Results of the Initial Neutronics and Thermal-Hydraulic Assessments," *INEEL Technical Report INEEL/EXT-03-00870, Rev. 1,* (2003).
5. D. M. McEligot and G. E. McCreery, "Scaling Studies and Conceptual Experiment Designs for NGNP CFD Assessment," lNEEL/EXT-04-02502, 30 November 2004.
6. K. G. Condie, G. E. McCreery, H. M. McIlroy Jr., and D. M. McEligot, "Development of an Experiment for Measuring Flow Phenomena Occurring in a Lower Plenum for VHTR CFD Assessment," INL/EXT-05-00603, 21 September 2005.
7. C. Stoots, S. Becker, K. Condie, F. Durst, and D. McEligot, "A Large-Scale Matched Index of Refraction Flow Facility for LDA Studies Around Complex Geometries," *Exp. in Fluids*, **30,** pp. 391-394 (2001).
8. C. Uzol, and C. Camci, "The Effect of Sample Size, Turbulence Intensity and Velocity Field on the Experimental Accuracy of Ensemble Averaged PIV Measurements," 4th International Symposium on PIV, Göttingen, Germany, Sep 17-19 (2001).
9. R. Volino and T. W. Simon, "Bypass Transition in Boundary Layers Including Curvature and Favorable Pressure Gradient Effects," *ASME J. Turbomachinery*, **117**, pp. 52-53 (1995).
10 W-J. Lee, K-D. Kim, M-K Hwang, H-S Lim, S-W Lee, T. Y. C. Wei, R. B. Vilim, E. E. Feldman, W. D. Pointer, R. R. Schultz, P. D. Bayless and R. L. Moore, "Generation of a Preliminary PIRT (Phenomena Identification and Ranking Table) for Very High Temperature Gas-Cooled Reactors," KAERI/TR-3050/2005, INL/EXT-05-00829, ANL-GenIV-066, September, 2005.